IEEE Access
Multidisciplinary ⋮ Rapid Review ⋮ Open Access Journal

Received 20 May 2023, accepted 31 May 2023, date of publication 9 June 2023, date of current version 16 June 2023.

Digital Object Identifier 10.1109/ACCESS.2023.3284684

RESEARCH ARTICLE

Four Degree-of-Freedom Hydrodynamic Maneuvering Model of a Small Azipod-Actuated Ship With Application to Onboard Decision Support Systems

MATHIAS MARLEY[1], (Member, IEEE), **ROGER SKJETNE**[1], (Senior Member, IEEE),
MATEUSZ GIL[2], AND **PRZEMYSLAW KRATA**[3,4]
[1]Department of Marine Technology, Norwegian University of Science and Technology, 7050 Trondheim, Norway
[2]Research Group on Maritime Transportation Risk and Safety, Faculty of Navigation, Gdynia Maritime University, 81-345 Gdynia, Poland
[3]Waterborne Transport Innovation Foundation, 80-173 Gdańsk, Poland
[4]Faculty of Mechanical Engineering and Ship Technology, Gdańsk University of Technology, 80-229 Gdańsk, Poland

Corresponding author: Mathias Marley (mathias.marley@ntnu.no)

This work was supported by the ENDURE project (NOR/POLNOR/ENDURE/0019/2019-00). ENDURE is supported by the Polish National Centre for Research and Development and by the Research Council of Norway (RCN). The work of Mathias Marley and Roger Skjetne was also partly supported by RCN through NTNU AMOS (RCN project 223254) and SFI AutoShip (RCN project 309230).

ABSTRACT The main contribution of this paper is a numerical ship motion model of NTNU's research vessel Gunnerus, capturing the surge, sway, roll, and yaw dynamics when sailing in uniform and steady currents. The model utilizes a crossflow drag formulation for the transverse viscous loads, and it includes a nonlinear formulation for the propulsion and steering loads provided by two azipod thrusters. A wide range of experimental data obtained from sea trials are used for model calibration and validation. The model is intended for development of Decision Support Systems (DSS) that provide the helmsman with recommendations for safe maneuvers. As a demonstration, the model is used to generate input to a previously proposed DSS solution, which uses offline simulations to create a database of the critical navigation area for different encounter scenarios. Additionally, we propose a DSS solution that uses online simulations to predict the future ship trajectory under guidance of a virtual autopilot. The virtual autopilot is designed using a novel hybrid control barrier function formulation to predict the need of evasive maneuvers for collision avoidance.

INDEX TERMS Hydrodynamic modeling, maneuvering model, maritime autonomous surface ships, decision support systems.

I. INTRODUCTION

A. BACKGROUND

The modern approach to design and operation of sociotechnical systems rely heavily on information technology and digitalization. Notable ongoing developments in the shipping industry is the rising level of autonomy of ships [1], and the introduction of digital twin solutions [2]. As the maritime transportation sector progresses towards Maritime Autonomous Surface Ships (MASS), there are expected benefits related to cost, safety, and sustainability. Vital to the development of MASS solutions is access to numerical simulation models that accurately predict ship motion responses over a wide range of operating conditions. Therefore, in this paper, we propose a 4 degree-of-freedom (4DOF) motion model of an azipod-actuated ship, where the model is valid at maneuvering speeds. Maneuvering models of ships that also include a high-fidelity representation of azipod thruster loads has so far not received much attention in literature. Models with podded propulsion units are presented for a large ship in [3], and [4], and for a small unmanned surface vessel (USV) in [5]. The latter model is used for

The associate editor coordinating the review of this manuscript and approving it for publication was Yanli Xu.

the development of a collision avoidance algorithm for USVs in [6].

As the use of azipod thrusters become more widespread, the demand for relevant studies is expected to increase. Since the first fully-operational MASS are likely to be limited in dimensions, our study focuses on a small but modern research vessel. Besides the development and validation of the numerical model, two applications of the motion model rooted in collision avoidance of a MASS are presented, with a view towards potential future application in onboard Decision Support Systems (DSS).

The work presented herein is part of the ENDURE research project on detection, prediction, and solutions for safe operations of maritime autonomous surface ships. A natural step towards increased ship autonomy is the use of intelligent onboard DSS serving the officer on watch. For this reason, a main focus of the ENDURE project is the development of DSS solutions that utilize online or offline numerical simulations of the ship motion to provide the officer on watch with safety-critical information. The Norwegian research vessel R/V Gunnerus (RVG) [8], [9] is used as a case study in ENDURE, along with the Polish research vessel Horyzont II [10]. RVG, depicted in Figure 1, is owned and operated by the Norwegian University of Science and Technology (NTNU) in Trondheim, Norway. She is equipped with two 500kW azipod thrusters at the stern, providing propulsion and turning capabilities during sailing. Originally, RVG had a length overall of 31.25 meters, but in 2019 she was elongated by adding a five meter section midship. The main parameters of RVG post-elongation are provided in Table 1; see also [11]. A three degree-of-freedom maneuvering model of RVG prior to elongation is provided in [12], and [13].

FIGURE 1. Illustration of RVG, courtesy of [7].

B. REVIEW OF MANEUVERING THEORY

Traditional maneuvering models capture the horizontal plane motions, and possibly also the roll motions, associated with turning maneuvers of ships. Maneuvering models may include the influence of uniform and steady currents, wind loads, and wave-drift loads, but do typically not include first-order wave-induced motions. We refer to [14], [15], and [16] for introductory reading on maneuvering theory.

TABLE 1. Main parameters of RVG.

Parameter	Value
Length overall	36.25 m
Length between perpendiculars	33.9 m
Breadth (middle)	9.6 m
Draft (moulded)	2.7 m
Lightweight	412 t
Deadweight	169 t

For ships moving at low or moderate Froude numbers, the fluid inertial loads associated with low-frequent motion are sufficiently represented by constant added mass matrices. The viscous loads, on the other hand, are considerably more challenging to model. This is particularly true for the transverse viscous loads, which are important for the ship response during hard turns [17].

Before continuing, let u_r and v_r be the fluid-relative velocities in surge and sway, respectively. For slender ships moving at small relative inflow angles, i.e., $|u_r| \gg |v_r|$, the hull may be modeled as a low-aspect-ratio lifting surface [15, Section 10.3.1]. This provides a good physical representation of the viscous loads encountered during steady sailing in low current velocities, but cannot be expected to be a good representation of the viscous loads during hard turns.

At large inflow angles, i.e., $|v_r| > |u_r|$, the crossflow drag principle is a suitable choice for the viscous loads in sway and yaw [15, Section 10.6.1]. In the crossflow drag method, the hull is divided into several sections, and the transverse drag load at each section is calculated from the local relative fluid velocity. An advantage of the crossflow approach is that coupling between sway and yaw motion is readily accounted for.

The underlying assumption of the crossflow principle is not valid under normal sailing conditions. An extension of the crossflow drag model to larger forward speeds, referred to as 2D+t theory, is presented in [15, Section 10.6.2]. In the 2D+t theory, the development of flow along the hull is accounted for by replacing the steady-state drag coefficients of the crossflow drag model with time-dependent drag coefficients. The authors of [17] compare crossflow drag and 2D+t formulations towards experimental data. While the 2D+t model provided the best overall fit towards the experiments, the crossflow drag model with modified drag coefficients yielded acceptable performance both at the initial stages of a turn, and during steady state turning.

C. CONTRIBUTIONS

The main contribution of this paper is a numerical ship motion model of RVG, consisting of two submodels; a 4DOF manueuvering model and a nonlinear actuator model. An illustration of the model architecture is provided in Figure 2. The maneuvering model is a physics-based model capturing the horizontal plane motion (surge, sway, and yaw), together with the roll motion induced by turning maneuvers.

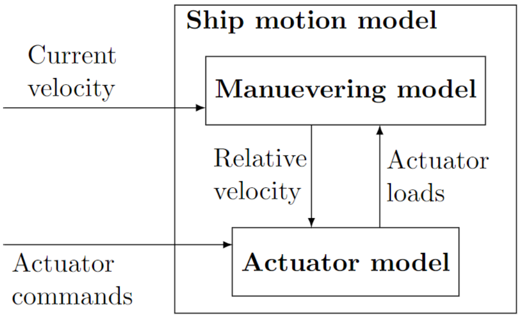

FIGURE 2. Architecture of the proposed ship motion model.

A crossflow drag formulation is used for the transverse viscous loads, whereas surge resistance is modeled using a quadratic drag formulation. The roll moments associated with turning are calculated based on the transverse loads, using the moment arm about the longitudinal axis for each of the respective load components. A similar approach for capturing roll motion was used in [18].

The actuator loads provided by the two azipod thrusters are calculated based on the propeller revolutions, azimuth angle, and relative fluid flow. Additionally, a first order model of the actuator dynamics is included, using the desired propeller revolutions and azimuth angles as inputs. The actuator model parameters are calibrated towards a functional mockup unit (FMU) model provided by the thruster supplier Kongsberg Maritime [11].

To calibrate the model, a set of sea trials were performed in the Trondheim fjord, consisting of turning circle tests and zig-zag tests performed at multiple forward speeds and azimuth angle executions. A simulation study reveals that the proposed model, including the actuator model, predicts the ship motion with reasonable accuracy over a wide range of operating conditions.

To illustrate potential uses of the numerical ship motion model, we study two conceptual solutions for DSS. The first solution, termed Critical Collision Avoidance Dynamic Critical Area, or CADCA for short, was originally proposed in [19], and [20]. The CADCA concept uses offline simulations to create a database of the critical navigation area for different encounter situations. The second solution is an online method, and uses a virtual autopilot with collision avoidance capabilities to predict and propose a safe ship trajectory. A novel hybrid control barrier function (CBF) formulation is used as basis for the virtual autopilot, building upon some of the authors previous work [21], [22], [23].

D. OVERVIEW OF PAPER

The main content of the paper is structured into model description, validation, and application as follows:

- **Model description:** The 4DOF maneuvering model and the actuator model are presented in sections II and III, respectively. Section III also presents the calibration of the actuator model towards the numerical model provided by the thruster supplier.
- **Model validation:** In Section IV, the ship motion model is calibrated and validated towards experimental results.
- **Model application:** Two examples of model applications are provided: The CADCA DSS solution is reviewed in Section V, whereas a CBF-based DSS concept is presented in Section VI.

A summary and discussion of the main results is provided in Section VII, whereas concluding remarks are provided in Section VIII.

II. 4DOF MANEUVERING MODEL

This section presents the 4DOF maneuvering model. The model is based on nonlinear maneuvering theory for the horizontal plane motion, whereas a small-angle assumption is employed for roll. The fluid loads associated with steady (time-invariant) and uniform (in space) currents are included. We select a pragmatic model structure of low complexity with basis in physical principles.

TABLE 2. Maneuvering model parameters.

Parameter	Symbol	Value	Unit
Length (between perpendiculars)	L_{pp}	33.9	m
Breadth	B_m	9.60	m
Draft	D_m	2.70	m
Mass	m	530	t
Roll radius of inertia	r_{44}	3.0	m
Yaw radius of inertia	r_{66}	9.0	m
Metacentric height	GM	2.03	m
Free surface correction	GM_{fsc}	0.3	m
Surge added mass coefficient	$C_{a,11}$	0.05	-
Sway added mass coefficient	$C_{a,22}$	0.4	-
Vertical ref. point added mass	z_a	1.98	m
Longitudinal ref. point added mass	x_a	-3.0	m
Vertical ref. point viscous loads	z_v	3.54	m
Sway linear damping	d_{22}	100	kN/(m/s)
Linear roll damping ratio	ζ_{44}	0.2	-
Surge base drag coefficient	$C_{x,0}$	0.12	-
Surge drag variation coefficient	$C_{x,1}$	0.2	1/rad
Sway drag coefficient	C_y	1.5	-

A. MODEL PARAMETERS

For convenience, all model parameters are provided in Table 2. Reasonable model parameters are selected based on engineering judgement, and then further refined by calibration towards experimental data. The model mass corresponds to a moderate ship loading condition. Strictly speaking, the model draft of 2.7 m does not correspond to the model loading condition of 530 t. This is of no significance, since the model length, breadth, and draft are merely used to calculate reference areas for the viscous loads, with the drag coefficients scaled towards the selected reference areas rather than the true projected areas. Further justification of the model parameters are provided as they are introduced.

B. NOTATION AND PRELIMINARIES

We consider a body-fixed right-handed coordinate system with x-axis pointing forward, z-axis pointing down, and reference origin at the center of gravity. An illustration of the inertial and body-fixed reference frames are provided in Figure 3. Consistent with hydrodynamic literature, see e.g. [14], we use index 1 for surge (longitudinal motion), 2 for sway (lateral motion), 4 for roll (rotation about longitudinal axis), and 6 for yaw (rotation about vertical axis).

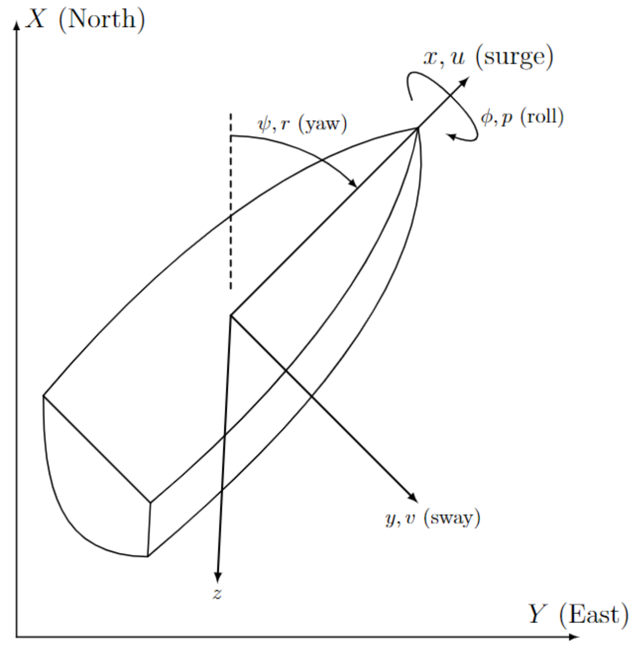

FIGURE 3. Inertial and body-fixed reference frames of the 4DOF manuevering model. Modified from [24].

$I_{n\times n}$ and $0_{n\times n}$ are the $n \times n$ identity matrix and zero matrix, respectively. We use the compact notation $\text{diag}(x_1, \dots, x_n)$ to denote a diagonal $n \times n$ matrix with $x_1, \dots, x_n$ along the diagonal. Lastly, $\text{atan2}(y, x)$ is the standard four-quadrant arctangent operation.

C. KINEMATICS

Let $\eta = [X \;\; Y \;\; \phi \;\; \psi]^T$ be the ship pose in the earth-fixed inertial reference frame, where (X, Y) is the horizontal plane position, ϕ is the roll angle, and ψ is the yaw angle (also referred to as ship heading). Let $\nu := [u \;\; v \;\; p \;\; r]^T$ be the body-fixed velocities, where u is the surge velocity, v is the sway velocity, p is the roll velocity, and r is the roll velocity. Define the planar rotation matrix $R(\psi)$ and 4DOF kinematic transformation matrix $T(\psi)$ as

$$R(\psi) := \begin{bmatrix} \cos(\psi) & -\sin(\psi) \\ \sin(\psi) & \cos(\psi) \end{bmatrix}, \tag{1}$$

$$T(\psi) := \begin{bmatrix} R(\psi) & 0_{2\times2} \\ 0_{2\times2} & I_{2\times2} \end{bmatrix}, \tag{2}$$

respectively. Assuming $\phi \approx 0$, the kinematic equation relating ship pose with body-fixed velocities is given by

$$\dot{\eta} = T(\psi)\nu. \tag{3}$$

D. CURRENT KINEMATICS

A uniform and steady current is described by the flow speed U_c, and the earth-fixed flow direction β_c. The inertial frame current velocity is then given by

$$\nu_c^n := U_c \left[\cos(\beta_c) \; \sin(\beta_c) \; 0 \; 0\right]^T, \tag{4}$$

whereas the body-fixed current velocity becomes

$$\nu_c := T(\psi)^T \nu_c^n. \tag{5}$$

Using $\dot{\nu}_c^n = 0$, the time-derivative of ν_c is obtained as

$$\dot{\nu}_c := \frac{d\, T(\psi)^T}{dt} \nu_c^n = r \begin{bmatrix} (SR(\psi))^T & 0_{2\times2} \\ 0_{2\times2} & I_{2\times2} \end{bmatrix} \nu_c^n, \tag{6}$$

where S is the 90-degree rotation matrix given by

$$S := \begin{bmatrix} 0 & -1 \\ 1 & 0 \end{bmatrix}. \tag{7}$$

E. EQUATION OF MOTION

Let

$$\nu_r := \nu - \nu_c \tag{8}$$

denote the fluid relative velocity in body-fixed coordinates. The equation of motion of the ship is stated as

$$M_{rb}\dot{\nu} + M_a\dot{\nu}_r + c_{rb}(\nu) + c_a(\nu_r) + d(\nu_r) + K\eta = \tau, \tag{9}$$

where M_{rb} and M_a are the rigid body and added mass matrices, respectively, $c_{rb}(\nu)$ and $c_a(\nu_r)$ are the rigid body and added mass Coriolis and centripetal loads, respectively, $d(\nu_r)$ is the hydrodynamic damping loads, K is a linear stiffness matrix, and τ collects the actuator loads. Eq. (9) can be solved using either ν or ν_r as the state. Choosing ν we obtain

$$\dot{\nu} = (M_{rb} + M_a)^{-1} \times (\tau - c_{rb}(\nu) - c_a(\nu_r) - d(\nu_r) - K\eta + M_a\dot{\nu}_c), \tag{10}$$

where $\dot{\nu}_c$ is given by (6).

F. RESTORING LOADS

Restoring loads act in roll only. In general, for a ship at forward speed, the restoring loads include hydrostatic and hydrodynamic effects, gravity effects, and free surface effects of fluid tanks. We neglect hydrodynamic effects, and assume linear stiffness, i.e.,

$$K := \text{diag}(0, 0, k_{44}, 0), \;\; k_{44} = mg(GM - GM_{fsc}), \tag{11}$$

where $g = 9.81$ m/s^2 is the acceleration of gravity, GM is the transverse metacentric height representative of the model loading condition, and GM_{fsc} is a correction term accounting for free surface effects. RVG is equipped with an anti-roll tank responsible for the main contribution to GM_{fsc}.

G. RIGID BODY INERTIA LOADS

For a ship with port-starboard symmetry, and reference origin at COG, the rigid body mass matrix becomes

$$M_{rb} := \mathrm{diag}(1, 1, r_{44}^2, r_{66}^2)m. \tag{12}$$

Here, m is the ship mass, whereas r_{44} and r_{66} are the inertia radii in roll and yaw, respectively. In lieu of accurate data, reasonable values for r_{44} and r_{66} are estimated from the overall ship dimensions. Neglecting Coriolis loads due to roll motion, the rigid body Coriolis loads are taken as

$$c_{rb}(\nu) := \left[-mvr \;\; mur \;\; 0 \;\; 0\right]^T. \tag{13}$$

H. FLUID INERTIA LOADS

In reality, the fluid inertia loads depend on the past motion of the ship, known as fluid-memory effects. Consistent with maneuvering theory, we represent the fluid inertia loads using constant added mass. As an initial estimate, frequency- and velocity-dependent added mass values were obtained using strip theory software. For maneuvering purposes, the added mass of the horizontal DOFs is often selected as the low-frequency asymptotic value at the service speed, whereas for roll motion and associated coupling terms the added mass corresponding to the roll natural period is likely to best capture the transient response during a turn. However, selecting the added mass according to the aforementioned rules failed to predict the ship motions recorded during sea trials. For this reason, the added mass values are instead estimated from the hull geometry using engineering judgement. The added mass matrix is assumed symmetric and on the form

$$M_a := \begin{bmatrix} a_{11} & 0 & 0 & 0 \\ 0 & a_{22} & a_{24} & a_{26} \\ 0 & a_{24} & a_{44} & 0 \\ 0 & a_{26} & 0 & a_{66} \end{bmatrix}. \tag{14}$$

The surge and sway added mass are taken as $a_{11} := C_{a,11}m$ and $a_{22} := C_{a,22}m$, respectively, where $C_{a,11}$ and $C_{a,22}$ are nondimensional added mass coefficients. The center of pressure of the fluid inertia forces are assumed acting at a reference point $(x_a, 0, z_a)$ in the body-fixed coordinate system, with z_a taken as the vertical center of buoyancy, and x_a located aft of midship, where the latter is justified by the twin skeg hull form of RVG. We further assume that the radii of inertia of the added mass about the added mass reference point corresponds to the rigid body inertia about COG. Under the aforementioned assumptions, the remaining added mass parameters are given by

$$\begin{aligned} a_{44} &:= a_{22}(r_{44}^2 + z_a^2), & a_{66} &:= a_{22}(r_{66}^2 + x_a^2), \\ a_{24} &:= -a_{22}z_a, & a_{26} &:= a_{22}x_a. \end{aligned} \tag{15}$$

The fluid Coriolis and centripetal loads are taken as

$$c_a(\nu_r) := \begin{bmatrix} -a_{22}v_r r - a_{26}r^2 \\ a_{11}u_r r \\ -a_{11}z_a u_r r \\ (a_{22} - a_{11})u_r v_r + a_{26}r^2 \end{bmatrix}, \tag{16}$$

where the contributions from roll motion are omitted, as before. Note that the roll term $-a_{11}z_a u_r r$ corresponds to the fluid Coriolis force in sway multiplied by a moment arm z_a. For 6DOF maneuvering models, the Coriolis moment in roll includes a term $-a_{15}u_r r$, where a_{15} is the surge-pitch added mass. Since $a_{15} \approx a_{11}z_a$, the two terms are consistent. We recognize the yaw moment term $(a_{22} - a_{11})u_r v_r$ as the Munk moment. Since $a_{22} \gg a_{11}$ for traditional ship geometries, the Munk moment is destabilizing, and important for the maneuvering capabilities of the ship.

I. HYDRODYNAMIC DAMPING LOADS

The hydrodynamic damping loads are modelled as

$$d(\nu_r) := D_l \nu_r + d_{nl}(\nu_r), \tag{17}$$

where D_l is a linear damping matrix, and

$$d_{nl}(\nu_r) := \left[d_{nl,1}(\nu_r) \;\; d_{nl,2}(\nu_r) \;\; d_{nl,4}(\nu_r) \;\; d_{nl,6}(\nu_r)\right]^T \tag{18}$$

represents the nonlinear loads.

1) SURGE RESISTANCE

The surge resistance is modelled by a quadratic drag formulation,

$$d_{nl,1}(\nu_r) = 0.5\rho C_x(\nu_r) A_x |u_r| u_r, \tag{19}$$

where $A_x := B_m T_m$ is the reference area, $\rho := 1.025\ t/m^3$ is the fluid density, and $C_x(\nu_r)$ is the flow-dependent drag coefficient. To better match the speed loss observed during turns in sea trials, $C_x(\nu_r)$ is selected as

$$C_x(\nu_r) := C_{x,0} + C_{x,1}|\mathrm{atan2}(v_r, u_r)|, \tag{20}$$

where $C_{x,0}$ is the base drag, and $C_{x,1} > 0$ gives an increase in the drag load proportional to the absolute value of the relative drift angle $\mathrm{atan2}(v_r, u_r)$.

2) CROSSFLOW DRAG MODEL

The viscous loads in sway and yaw, as well as the sway-induced roll moment, is calculated using a crossflow drag model. Let C_y be the transverse drag coefficient, assumed constant along the hull and normalized by the design draft T_m, and let

$$v_l(x, \nu_r) = v_r + xr - z_v p \tag{21}$$

be the local transverse fluid relative velocity. Here, z_v is the vertical reference coordinate for the viscous fluid loads. The drag loads in sway and yaw are obtained by integrating along the hull,

$$d_{nl,2}(\nu_r) := \int_{x_s}^{x_b} 0.5\rho C_y T_m |v_l(x, \nu_r)| v_l(x, \nu_r) dx, \tag{22}$$

$$d_{nl,6}(\nu_r) := \int_{x_s}^{x_b} 0.5\rho C_y T_m |v_l(x, \nu_r)| v_l(x, \nu_r) x dx, \tag{23}$$

where x_s and x_b are the longitudinal coordinates of the stern and bow, respectively. Assuming $d_{nl,2}(\nu_r)$ acts at the reference elevation z_v, we obtain the roll moment about the origin as

$$d_{nl,4}(\nu_r) := -d_{nl,2}(\nu_r)z_v. \tag{24}$$

This captures the sway-induced viscous roll moment during turning. Additionally, since the roll-induced sway velocity is included in the calculation of $v_l(x, \nu_r)$, it includes a dissipative moment in roll. This is perhaps unphysical, since the flow may not have time to develop for oscillatory roll motions. However, the overall roll damping level is calibrated using the linear damping. The cross flow drag model is implemented with $x_b := -L_{pp}/2$, $x_s := L_{pp}/2$, and numerically integrating over 15 sections of equal length. To replicate the roll response of the sea trials, z_v is taken as the elevation of the keel.

3) LINEAR DAMPING

An outcome of the model calibration is additional linear damping in sway and roll, i.e.,

$$D_l := \begin{bmatrix} 0 & 0 & 0 & 0 \\ 0 & d_{22} & d_{24} & 0 \\ 0 & d_{42} & d_{44} & 0 \\ 0 & 0 & 0 & 0 \end{bmatrix}. \tag{25}$$

The roll-sway coupling terms are taken as $d_{42} := d_{24} := -z_v d_{22}$, which assumes that the sway linear damping force acts at the same elevation as the viscous forces. A physical explanation for the additional sway damping needed to match the sea trials is yet to be identified. The linear roll damping is related to a critical damping ratio ζ_{44} (assuming uncoupled roll motion) by specifying d_{44} as $d_{44} := 2\zeta_{44}\sqrt{k_{44}(mr_{44}^2 + a_{44})}$. The main source of the linear roll damping is assumed to be the bilge keels and the anti-roll tank.

III. ACTUATOR MODEL

Kongsberg Maritime has provided an FMU model of the azimuth thrusters, available at the Open Simulation Platform [25]. Due to a desire for a standalone numerical model that does not rely on external software, a simplified actuator model is calibrated towards the FMU results. The simplified actuator model assumes that the propulsion and steering loads can be represented by a naive calculation of the thrust force that depends only on propeller revolutions, in combination with drag and lift loads acting on a virtual foil. The virtual drag and lift loads account for the change in thrust force magnitude and direction due to fluid inflow, in addition to the true drag and lift loads on the propeller body.

A. MODEL STRUCTURE

In the following, we consider a single azipod thruster located at (x_t, y_t, z_t) in body-fixed coordinates, with the transverse position $y_t = \pm 2.7$ depending on the thruster. The actuator loads are calculated using the azimuth angle α, propeller revolutions ω, and the relative fluid flow ν_r as inputs. For notational simplicity, most functions below are provided without their arguments. An illustration of the actuator load model is provided in Figure 4. The thrust force F_t is assumed quadratic in propeller revolutions ω, i.e.,

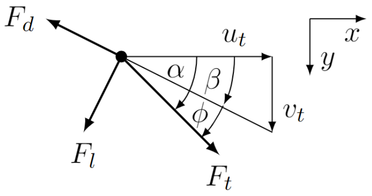

FIGURE 4. **Illustration of actuator force model.**

$$F_t := C_t\omega^2, \tag{26}$$

where C_t is the thrust force coefficient. Disregarding the influence of roll, the fluid relative surge and sway velocities at the thruster location are given by

$$u_t := u_r - y_t r, \quad v_t := v_r + x_t r, \tag{27}$$

respectively. The flow orientation β in the body-fixed reference frame, and total fluid flow velocity V becomes

$$\beta := \text{atan2}(v_t, u_t), \quad V := \sqrt{u_t^2 + v_t^2}, \tag{28}$$

respectively. The fluid angle of attack ϕ, relative to the thruster orientation α, is then obtained as

$$\phi := \alpha - \beta. \tag{29}$$

We calculate the (virtual) drag F_d and lift F_l as

$$F_d = 0.5\rho A_p C_d(\phi)V^2, \quad F_l = 0.5\rho A_p C_l(\phi)V^2, \tag{30}$$

where A_p is a reference area. The lift coefficient $C_l(\phi)$ and drag coefficient $C_d(\phi)$ are taken as

$$C_l(\phi) := \quad 0.5\, C_{l,1}\sin(2\phi), \;\; C_d(\phi) := C_{d,0} + C_{d,1}|\phi|. \tag{31}$$

respectively. Here, $C_{d,0}$ is the base drag coefficient, whereas $C_{d,1}$ and $C_{l,1}$ account for the variations in the drag and lift coefficients as a function of ϕ. Note that, for small ϕ, the lift coefficient $C_l(\phi)$ is linear in ϕ with slope $C_{l,1}$.

By definition, F_d and F_l act inline with and perpendicular to the relative fluid velocity, respectively, whereas the thrust force F_t is assumed acting in the propeller direction. Decomposing F_t, F_d, and F_l into the body-fixed reference frame, we obtain the actuator loads as

$$\begin{aligned} \tau &:= \begin{bmatrix} \tau_1 & \tau_2 & \tau_4 & \tau_6 \end{bmatrix}^T, \\ \tau_1 &:= F_t\cos(\alpha) - F_d\cos(\beta) - F_l\sin(\beta), \\ \tau_2 &:= F_t\sin(\alpha) - F_d\sin(\beta) + F_l\cos(\beta), \\ \tau_4 &:= -z_t\tau_2, \\ \tau_6 &:= x_t\tau_2 - y_t\tau_1. \end{aligned} \tag{32}$$

The total actuator loads are obtained by repeating the calculation steps (26)-(32) for both thrusters, and summing these up.

B. FIRST ORDER ACTUATOR DYNAMICS

The actuator dynamics are given by a rate-limited first order model,

$$\dot{\alpha} = -\operatorname{sat}\left(\frac{\alpha - \alpha_d}{t_\alpha}, \dot{\alpha}_{max}\right), \tag{33a}$$

$$\dot{\omega} = -\operatorname{sat}\left(\frac{\omega - \omega_d}{t_\omega}, \dot{\omega}_{max}\right), \tag{33b}$$

where subscript d denote the desired actuator state, t_α and t_ω are time constants, and $\dot{\alpha}_{max}$ and $\dot{\omega}_{max}$ are the rate limits. The saturation function is defined as $\operatorname{sat}(s, a) := \operatorname{sign}(s)\min(|s|, a)$.

TABLE 3. Actuator model parameters.

Parameter	Symbol	Value	Unit
x-coordinate	x_t	-16.95	m
y-coordinate	y_t	± 2.7	m
z-coordinate	z_t	4.54	m
Thrust force coefficient	C_t	0.0022	kN/RPM^2
Virtual foil reference area	A_{ref}	9	m^2
Base drag coefficient	$C_{d,0}$	0.3	-
Drag variation coefficient	$C_{d,1}$	0.3	-/rad
Lift variation coefficient	$C_{l,1}$	0.5	-/rad
Azimuth angle time constant	t_α	1	1/s
Revolutions time constant	t_ω	1	1/s
Azimuth angle rate limit	$\dot{\alpha}_{max}$	$\pi/6$	rad/s
Propeller revolutions rate limit	$\dot{\omega}_{max}$	20	RPM/s.

C. ACTUATOR MODEL CALIBRATION

The thrusters are located near the stern, at a distance 2.7m port and starboard of centerline. Actuator model parameters are provided in Table 3. The longitudinal and lateral thruster coordinates are taken as the position of the azimuth axis, whereas the vertical coordinate is tuned to replicate the roll motion of the sea trial results. In lieu of data, the time constants and rate limits are selected using engineering judgement. The remaining parameters are calibrated towards the FMU dataset, over a wide range of flow conditions, azimuth angles, and propeller revolutions. A sample comparison for selected data points is provided in Figure 5. Note, in particular, that the calibration data and the model presented herein predict the same slope and zero-crossing of the sway force as a function of azimuth angle. The largest discrepancy is observed in the surge force for the maximum propeller revolutions of $\omega = 220$ RPM. Overall, the "thrust+virtual foil" model structure qualitatively captures the variations in actuator loads due to change in azimuth angle, propeller revolutions, and fluid flow.

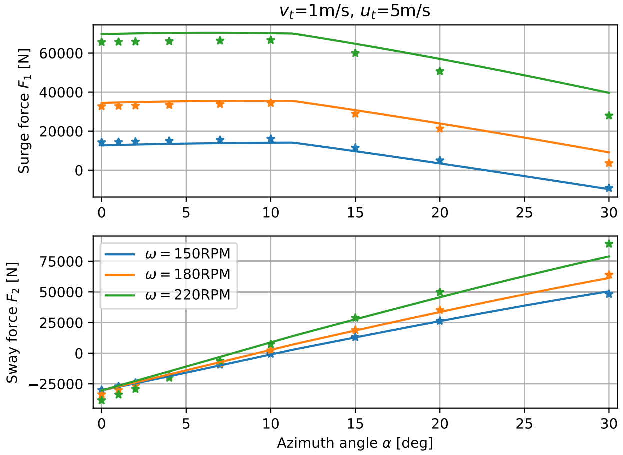

FIGURE 5. Actuator loads versus azimuth angle, for selected flow condition $u_t = 5$ m/s, $v_t = 1$ m/s, and varying propeller revolutions. The gradient of F_1 is discontinuous for $\alpha = \beta = \operatorname{atan2}(v_t, u_t) \approx 11.31$ deg.

IV. MODEL CALIBRATION AND VALIDATION

A set of maneuvering tests were performed on a very calm day, the 27th October 2022, in the Trondheim fjord, providing the sea trials dataset used for model calibration and validation. An overview of the performed tests is obtained by examining figures 7 and 6.

A. METHODOLOGY

The commanded propeller revolutions and azimuth angles obtained from the sea trials dataset are applied as the desired propeller revolutions and azimuth angles in numerical simulations; see Figure 7. A subset of the sea trials, more specifically the time period marked as 1500s to 3200s, is selected as a focus period for the model calibration. During this time period, RVG was operated with 170RPM, corresponding to normal cruising speed, and moderate azimuth angles of ± 10 degrees. The remainder of the dataset is used mainly for validation. A constant current of 0.15m/s towards East is applied in the numerical simulations. This corresponds to an estimate of the average current conditions encountered during sea trials. To ensure alignment between real-life and simulated ship headings, the model pose is reset at uneven intervals.

B. RESULTS

A comparison of the sea trial trajectory and the numerically simulated trajectory is shown in Figure 6. Significant discrepancy in the trajectories is expected due to cumulative (drift) errors during time integration, as well as unmodelled environmental disturbances.

Time series of surge and sway velocities are provided in Figure 8. Good correspondence is observed both for the speed loss during turning, and the fluctuations in surge velocity due to currents. For large propeller revolutions, $\omega > 200$ RPM, the numerical model overestimates the surge velocity. The sea

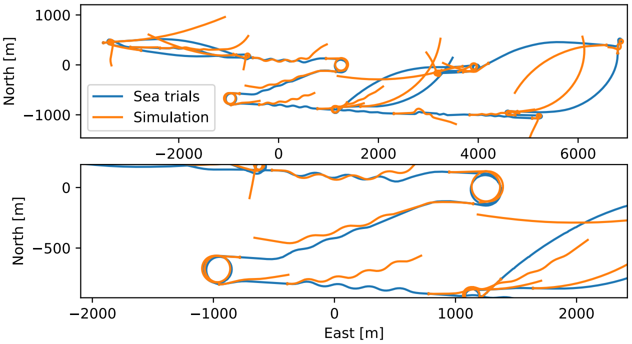

FIGURE 6. **Trajectories from sea trials and simulations, for the full dataset duration (top), and for the focus period 1500s to 3000s (bottom). The model pose is reset to the sea trials data at uneven intervals, resulting in discontinuities in the simulated trajectories.**

trial sway velocity has a mean offset that does not correlate with ship heading, and thus is not easily explained by environmental loads. Possible explanations are bias in the measurements, or a small drift velocity caused by actuator bias. The perturbations about the mean sway velocity compare reasonably well, with a slight tendency of the numerical model to overestimate turning-induced drift velocities. Comparison of heading rates and roll angles is shown in Figure 9. For the sea trials data there is a small mean offset in the roll angle. Both the time scale of the dynamic transients, as well as the signal amplitudes, show good correspondence.

As stated previously, model calibration is performed with a focus on the time period from 1500 to 3200s. Yet, the model predicts the ship motion with reasonably accuracy over the full set of operating conditions considered during sea trials. Justified by its basis in physical principles, the 4DOF maneuvering model is expected to have a large validity range, perhaps even extending beyond the sea trials dataset. However, the actuator model cannot be expected valid beyond the calibration data, limiting the overall validity range of the ship motion model.

V. DSS USING THE CADCA CONCEPT

To illustrate the practical usability of the ship motion model, a set of simulated trajectories are used to a create a CADCA (Collision Avoidance Dynamic Critical Area) database. The CADCA database provides the minimal required maneuvering areas of the ship with respect to both static and dynamic obstacles, taking the restrictions on allowable heel angles into account. A detailed description of the concept, including its research assumptions, calculation procedure, limitations, and the vast set of simulation results for various ship models, is given in [19], and [20].

A. THE CADCA CONCEPT

The CADCA concept indicates the last distance between the active ownship (executing a single action) and a passive target ship (maintaining its course and speed), at which the evasive maneuver should be executed to avoid a collision. This distance called MDTC (Minimum Distance to Collision) is calculated for a given set of operational and environmental conditions, including azimuth angle (or rudder) execution, initial forward speed, course alteration, and wave conditions (still-water conditions are assumed for the results presented herein). As the CADCA is calculated using simulated trajectories on a 4DOF model, it allows for consideration of ship motions and maneuverability during the collision-avoidance process. Through this, it may take into account not only the geometrical characteristic of close-quarter situations, but also provides access to the ship stability indicators during the process of planning evasive maneuvers [26]. Such a complex approach may be beneficial in the context of MASS, where leading safety or risk indicators will be used to predict various aspects of ship operation [27], including ship stability and encounter parameters [28]. If safety or risk indicators are expected to be violated, an autonomous vessel may take an action or warn human operators at a remote Shore Control Center (SCC) [29].

B. EXEMPLARY RESULTS

Figure 10 depicts the CADCAs determined for exemplary encounter scenarios, with ownship trajectories provided by the model presented herein. The critical areas are presented for RVG versus a stationary obstacle enlarged by a 500 m safety zone that typically surrounds offshore installations, and RVG versus Horyzont II as target ship. The target ship domain is given by the decentralized elliptical domain with dimensions as given in [30], which is inspired by Coldwell's ship domain [31].

The CADCAs presented in Figure 10 A are determined for different settings of azimuth (rudder) angle when RVG proceeds at 8.5 kts and executes a turn to the starboard side by 60 degrees. In Figure 10 B, RVG at 12 kts encounters the target underway (ship domain) having a forward speed of 8.5 kts. In this simulation scenario, RVG turns to the port side by deflecting the azipod by 10 degrees while the course alterations for each evasive maneuver differ. The ship encounters in which the single maximum MDTCs were calculated for both aforementioned scenarios (for data series marked in brown) are presented with ship trajectories, overlaid CADCAs, and key maneuvering parameters in Figure 11.

VI. DSS USING A VIRTUAL AUTOPILOT

We propose a DSS concept that uses online predictions of the future ship trajectory under the guidance of a virtual autopilot. The predicted ship trajectory serves as a proposed trajectory for the officer on watch. By simulating on the high-fidelity model, we ensure that the proposed trajectory is feasible. The proposed DSS assumes, as a worst case scenario, that each identified target ship will sail on constant course and speed based on the most recent AIS information. As time moves on, the updated AIS information is repeatedly applied to recalculate the predicted trajectories, thus accounting for

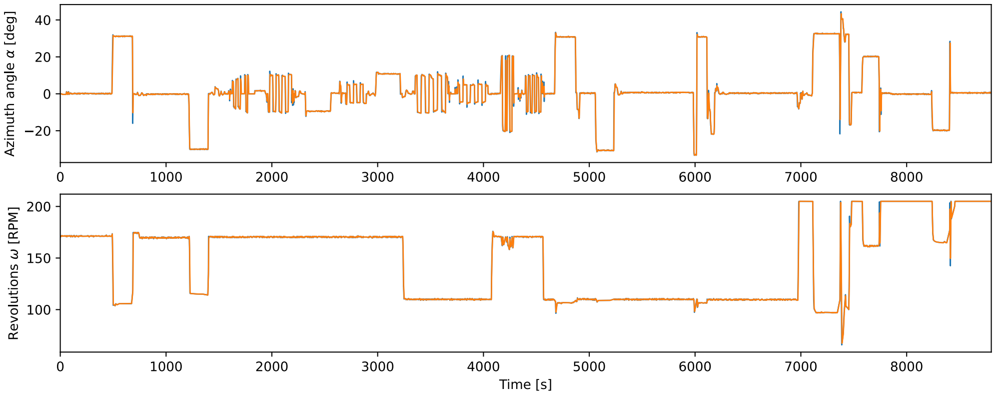

FIGURE 7. Sea trial azimuth angle and propeller revolutions (blue), and commanded azimuth angle and propeller revolutions in the numerical simulations (orange.).

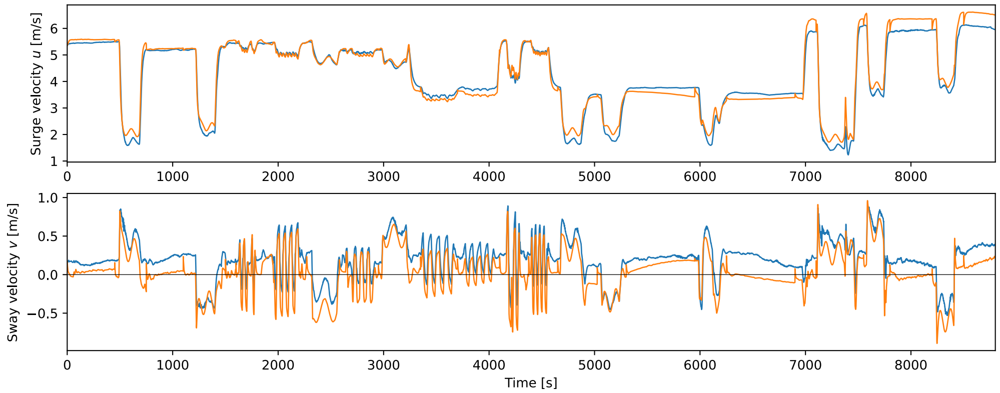

FIGURE 8. Surge velocities (top) and sway (bottom) from sea trials (blue) and simulation (orange).

changes in target ship maneuvers, such as give-way course changes.

A. PRELIMINARIES

In this section, we use a more rigorous mathematical notation than the previous sections of the paper, consistent with [22], and [23]. $\mathbb{N}$ is the set of integers, $\mathbb{R}$ is the set of real numbers, $\mathbb{R}_{\geq 0}$ is the set of nonnegative numbers, and $\mathbb{R}^n$ is the n-dimensional Euclidean space. The Euclidean norm of a vector $x \in \mathbb{R}^n$ is denoted $|x|$. For two column vectors $x_1 \in \mathbb{R}^{n_1}$, $x_2 \in \mathbb{R}^{n_2}$, we occasionally use the compact notation $(x_1, x_2) := [x_1^T \;\; x_2^T]^T \in \mathbb{R}^{n_1+n_2}$. We denote by $\mathbb{S}^1 := \{x \in \mathbb{R}^2 : x^T x = 1\}$ the unit circle. For a scalar function $B : \mathbb{R}^n \times Q \to \mathbb{R}$ we use the Lie derivative notation,

$$L_f B(x, q) := \frac{\partial B(x, q)}{\partial x} f(x), \tag{34}$$

to denote the directional derivative of B, with respect to its first argument, along a vector field $f : \mathbb{R}^n \to \mathbb{R}^n$.

B. GUIDANCE CONTROL DESIGN

We design a guidance control algorithm that takes the ship position, surge speed, and heading angle as inputs, and outputs the desired heading rate. A hybrid CBF design is used for collision avoidance, with target ships assumed to maintain a constant velocity given by the latest AIS information. The algorithm builds upon our previous work on hybrid feedback control applied to obstacle avoidance for underactuated ships [21], safe maneuvering control using nonhybrid CBFs [23], and hybrid CBFs applied to obstacle avoidance of nonholonomic vehicles [22]. We refer to [32] for introduction to CBF theory.

The obstacle avoidance designs in [21], [22], and [23] considers only static circular obstacles. While dynamic obstacles are readily accommodated by CBF theory, on should note that only the velocity components along the straight line between the ownship and the target ship is taken into account. As such, CBFs lack any predictive behavior or sophisticated problem-solving ability. A CBF design for fully actuated ships that complies with collision regulations at sea (COLREGs) is proposed in [33], using a dynamic half-plane separation approach, where the dividing line of the two half-planes rotate as the ships pass.

We propose a hybrid CBF formulation that uses a logic variable to select between overlapping CBF-like functions, each defining a half-plane constraints with fixed orientation.

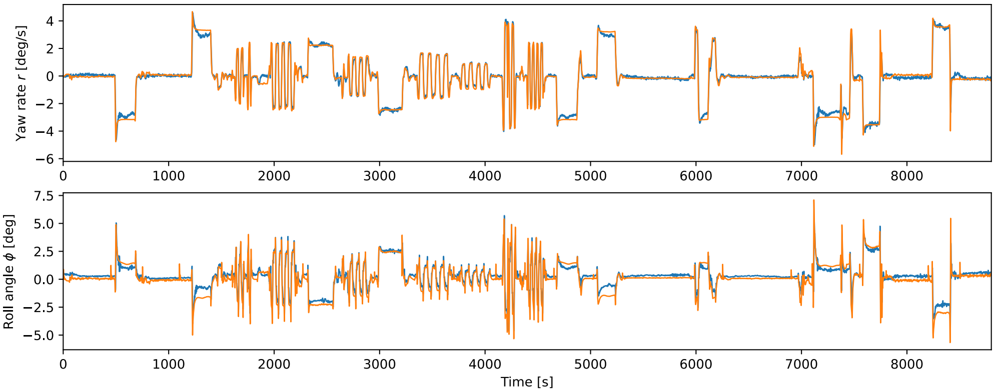

FIGURE 9. Heading rate (top) and roll angle (bottom) from sea trials (blue) and simulation (orange).

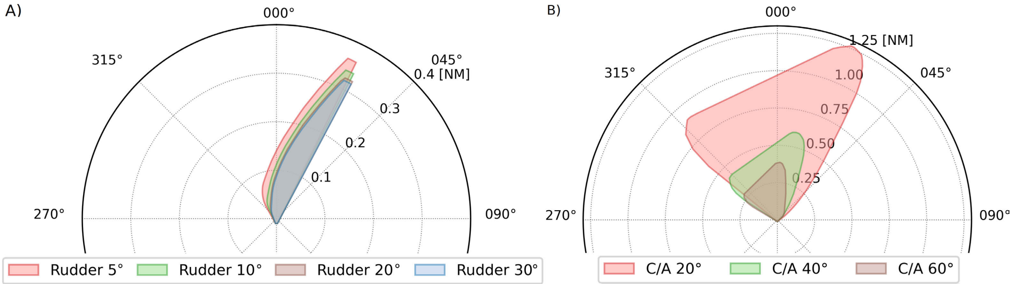

FIGURE 10. The CADCAs determined using the RVG ship motion model for different azimuth angles and encounters with a stationary obstacle (part A), as well as for different course alterations (part B) in encounters with the target underway.

The resulting hybrid CBF defines a polygon ship domain, with polygon shape selected such that the ship performs predictable and deliberate evasive maneuvers when encountering target ships. The algorithm is currently at a conceptual level, and relies on proper designation of the collection of half-plane constraints depending on the encounter scenario. A systematic procedure for selecting the half-plane constraints is considered future work and beyond the scope of this paper.

1) CONTROL DESIGN MODEL

The guidance control law is implemented on a kinematic level with the ship kinematics represented by a unicycle model moving at constant forward speed, and using the desired heading rate $r_d \in \mathbb{R}$ as a control input. The unicycle representation implicitly assumes sway velocity $v \equiv 0$, and omits the influence of speed loss during turning. For consistency with earlier work we adopt the unit circle representation of orientation [34]. Let $p := (X, Y) \in \mathbb{R}^2$, $z := (\cos(\psi), \sin(\psi)) \in \mathbb{S}$ and $u \in \mathbb{R}_{\geq}0$ be the position, heading, and forward speed of the ownship, respectively. We consider a single target ship with position $p_o \in \mathbb{R}^2$, moving at a constant forward speed $u_o \in \mathbb{R}pos$ at constant course $z_o \in \mathbb{S}one$. where subscript o denotes obstacle. The control design model, including target ship dynamics, are formulated as the affine control system

$$\dot{x} = \begin{bmatrix} \dot{p} \\ \dot{p}_o \\ \dot{z} \end{bmatrix} = \begin{bmatrix} zu \\ z_o u_o \\ 0_{2\times 1} \end{bmatrix} + \begin{bmatrix} 0_{2\times 1} \\ 0_{2\times 1} \\ Sz \end{bmatrix} r_d =: f(x) + g(x) r_d, \tag{35}$$

with state $x := (p, p_o, z) \in \mathbb{R}^2 \times \mathbb{R}^2 \times \mathbb{S}one \subset \mathbb{R}^6$, and input $r_d \in \mathbb{R}$.

C. CBF DESIGN

Let $Q \subset \mathbb{N}$ be a finite set, let $q \in Q$ be a logic variable, and define the scalar function $B_1 : \mathbb{R}^6 \times Q \to \mathbb{R}$ as

$$B_1(x, q) := d_q - \tau_q^T (p - p_o). \tag{36}$$

For each fixed q, the zero sublevel set

$$\{x \in \mathbb{R}^6 : B_1(x, q) \leq 0\} \tag{37}$$

represents a half-plane constraint with distance parameter $d_q > 0$, and unit normal vector $\tau_q \in \mathbb{S}one$, referred to as the orientation. The set in (37) is commonly referred to as the safe set in CBF literature. We assume the distance parameters are selected such that $|p - p_o| > \min_{q \in Q} d_q$ implies that the ships are not in contact, including a robustness margin. The collection of half-plane constraints form a Target Ship

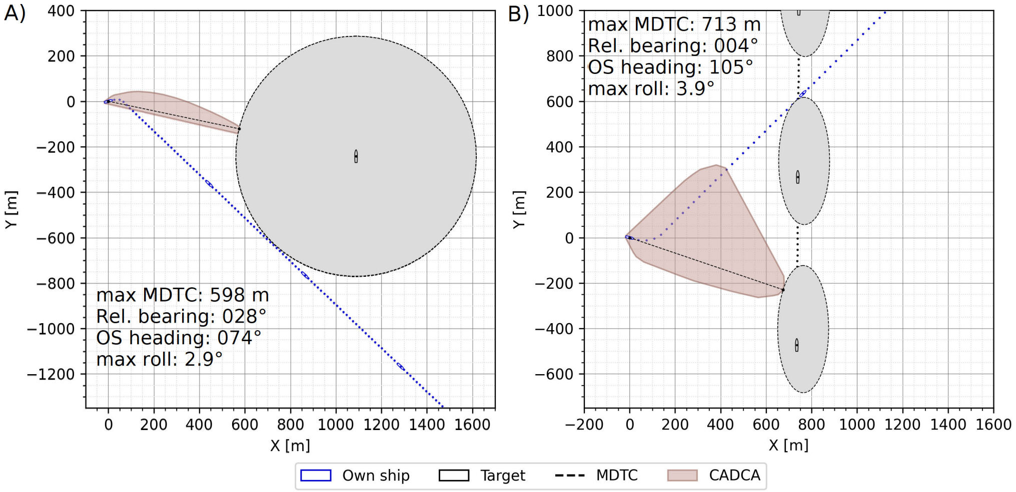

FIGURE 11. The ship trajectories corresponding to the cases in which the single maximum MDTCs were determined in the analyzed scenarios (for data series marked in brown) with overlaid CADCAs.

Critical Area ($TSCA$) given by

$$TSCA(p_o) := \{p \in \mathbb{R}^2 : B_1(x, q) > 0 \quad \forall q \in Q\}, \tag{38}$$

where the parameter set $\{(d_q, \tau_q) : q \in Q\}$ is selected such that $TSCA(p_o)$ forms a closed convex polygon. Collision avoidance is then achieved by steering the own-ship such that it stays clear of $TSCA(p_o)$, i.e., by enforcing $p(t) \notin TSCA(p_o(t))$ for all $t \geq 0$. Since $p \in TSCA(p_o) \implies B_1(x, q) > 0$, this is equivalent to maintaining $B_1(x(t), q(t)) \leq 0$ for all $t \geq 0$.

The key idea behind CBFs is to enforce safety by restricting the evolution of B_1 along the system (35). However, since $L_g B_1(x, q) = 0$, we have no direct control over $\dot{B}_1 = L_f B_1(x, q)$. Instead, we backstep the CBF by defining a second function $B_2 : \mathbb{R}^6 \times Q \to \mathbb{R}$ as [35], and [36]

$$B_2(x, q) := L_f B_1(x, q) + \gamma_1 B_1(x, q), \tag{39}$$

where $\gamma_1 > 0$ is a tuning parameter. B_2 is used to identify an input set

$$\begin{aligned} U_B(x, q) &: = \{r_d \in \mathbb{R} : \dot{B}_2(x, q, r_d) \leq -\gamma_2 B_2(x, q)\}, \\ \dot{B}_2(x, q, r_d) &: = L_f B_2(x, q) + L_g B_2(x, q) r_d, \end{aligned} \tag{40}$$

with tuning parameter $\gamma_2 > 0$. For each $(x, q) \in \mathbb{R}^6 \times Q$, $U_B(x, q)$ is the set of inputs such that the evolution of B_2 along (35) satisfies $\dot{B}_2 \leq -\gamma_2 B_2$.

1) SAFEGUARDING CONTROL LAW

The state-dependent input constraint (40) may be synthesized with any nominal control law by always selecting the safe input that is closest to the nominal input, i.e., by defining the safeguarding control law

$$r_{d,safe}(x, q) := \arg \min_{r_d \in U_B(x,q)} |r_d - r_{d,nom}(x)|. \tag{41}$$

where $r_{d,nom} : \mathbb{R}^6 \to \mathbb{R}$ is a nominal control law. For the DSS we select the nominal control law [34]

$$r_{d,nom}(z) := \frac{-k_1 \tilde{z}_2}{\sqrt{1 - \lambda^2 \tilde{z}_1^2}}, \quad \tilde{z} := \begin{bmatrix} z_d & S z_d \end{bmatrix}^T z, \tag{42}$$

$k_1 > 0$, $0 < \lambda < 1$, which regulates the ship heading to a constant desired heading $z_d := (\cos(\psi_d), \sin(\psi_d)) \in \mathbb{S}one$.

2) SWITCHING LOGIC

For each fixed q, the closed-loop system (35),(41)-(42) moves within the set $\{x : B_1(x, q) \leq 0\}$. What remains is to design a logic for proper switching of the active safety constraint. Let q^+ denote the value of q after a switch. We propose a dynamic update law for q based on bounded increase of B_1 and strict decrease of B_2. In particular, we require that, whenever q toggles, the inequalities

$$B_1(x, q^+) \leq \max\{0, B_1(x, q)\}, \tag{43a}$$
$$B_2(x, q^+) \leq B_2(x, q) - \delta, \tag{43b}$$

are satisfied, with hysteresis width $\delta > 0$. Note that the requirement of strict decrease of B_2 prevents chattering, since it excludes the possibility of consecutive switches between two values of q. Define

$$\begin{aligned} H_1(x, q) &: = \{h \in Q : B_1(x, h) \leq \max\{0, B_1(x, q)\}\}, \\ H_2(x, q) &: = \{h \in Q : B_2(x, h) \leq B_2(x, q) - \delta\}, \\ H(x, q) &: = H_1(x, q) \cap H_2(x, q), \end{aligned} \tag{44}$$

which identifies the subset of q such that (43) is satisfied. The switching logic is then formally stated as

$$\begin{aligned} &\text{if} \quad H(x, q) \neq \emptyset : \\ &q^+ \in G(x, q) : = \arg \min_{h \in H(x,q)} B_2(x, h). \end{aligned} \tag{45}$$

In the rare case that $G(x, q)$ is not unique, q^+ is selected at random.

D. IMPLEMENTATION AS DSS CONCEPT

The guidance control algorithm formed by the safeguarding control law (41)-(42), in combination with the switching logic (44)-(45), is used as a virtual autopilot for predicting the future ship motion. Simulations are performed on the 4DOF ship motion model, with the desired azimuth angle applied as

$$\alpha_d = -k_2(r - r_{d,safe}(x, q)) + k_3 r_{d,safe}(x, q), \qquad (46)$$

where $k_2 > 0$ is a feedback gain, and $k_3 > 0$ is a velocity feedforward gain. When run on a standard laptop (Dell Latitude 7400 with an Intel Core i7-8665U 1.9 GHz processor), a 10 minute simulation takes less than 1 second CPU time, meaning the predicted trajectories may be updated every few seconds. Following each simulation, key information may be reported to the helmsman, such as predicted time to evasive maneuver, required azimuth angle execution, and peak roll angle.

To illustrate the proposed DSS concept, we consider two scenarios. In the first scenario, see Figure 12, a target ship is approaching from port. According to COLREGs, the ownship shall stand its course, whereas the target ship shall give way. The shape of $TSCA(p_o)$ is selected to enforce a portside turn for the ownship if the target ship does not obey COLREGs. Here, we note that a full turning circle toward starboard would be the typical evasive maneuver when the target ship does not obey COLREGs. However, in close-quarter situations a portside turn solution, as presented in Figure 11 B, may be applied under exceptional circumstances. In the second scenario, see Figure 13, the ownship and target ship are on head-on collision course. The shape of $TSCA(p_o)$ is selected to enforce a starboard turn, giving the target ship sufficient space to pass port without altering its course.

For both scenarios, the target ship alters it course as time evolves. Snapshots of the encounter situations are shown at 30 s intervals. The time to evasive maneuver (TTEM) is predicted using the latest (simulated) AIS data for target ship course and speed. For each snapshot, the ownship position $p(t)$ and target ship position $p_o(t)$ at the present time t are shown as blue and orange ships, respectively. The corresponding past trajectories and predicted future trajectories are shown as solid and dashed curves, respectively. The black ship, red ship, and red polygon indicate the predicted $p(t + \text{TTEM})$, $p_o(t + \text{TTEM})$, and $TSCA(p_o(t + \text{TTEM}))$, respectively, at time $t + \text{TTEM}$. The red dotted line indicates the active half-plane constraint at the start of the evasive maneuver. Since the ownship is not allowed to cross the active half-plane constraint, a turn is forced. Later the active constraint switches, enabling the ownship to pass behind the target ship. Observe that the evasive maneuvers are initiated before the ownship reaches the boundary of the predicted target ship critical area, giving the ownship ample time for evasive action. This is an inherent property of the CBF-based guidance control design, which restricts the allowed convergence rate between p and $TSCA(p_o)$.

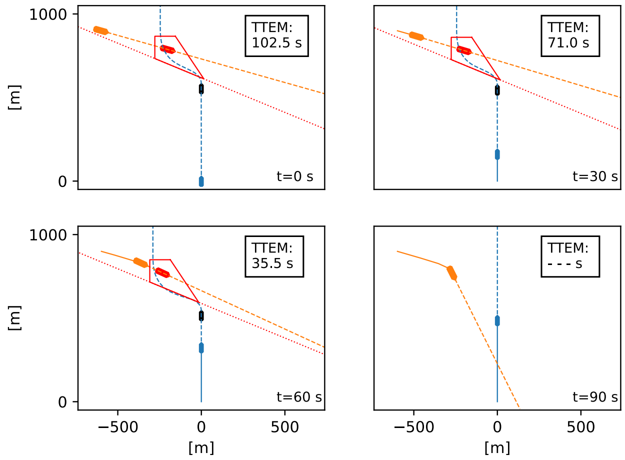

FIGURE 12. **Illustration of the crossing encounter scenario. At time $t = 90$ s, the target ship has altered its course, and no evasive action is required from ownship. In this situation, the virtual autopilot proposes a portside turn if the give-way vessel does not adhere to COLREGs, whereas the safest maneuver would typically be a full circle to starboard. The figure serves to illustrate the proposed DSS solution, while further development of the virtual autopilot is necessary before deployment.**

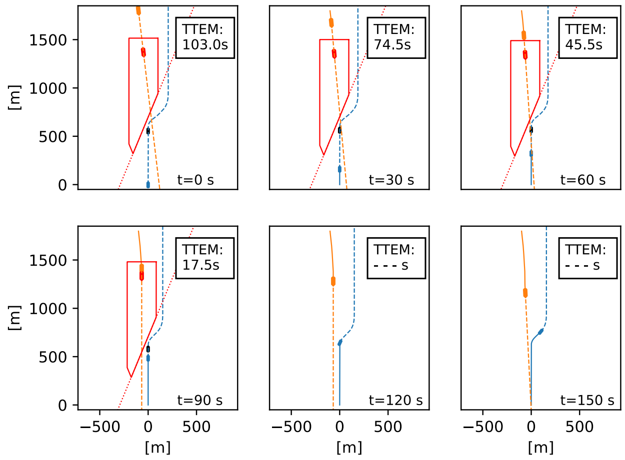

FIGURE 13. **Illustration of the head-on encounter scenario. At time $t = 120$s, the helmsman is assumed to have initiated an evasive maneuver as recommended by the virtual autopilot.**

VII. SUMMARY AND DISCUSSION

A. SHIP MOTION MODEL

A 4DOF maneuvering model of RVG based on well-known maneuvering theory was presented in Section II, whereas a nonlinear actuator model was presented in Section III. The maneuvering model includes fluid loads associated with uniform and steady currents, and uses a crossflow drag formulation for the transverse viscous loads. The actuator model was calibrated towards an FMU model provided by the thruster supplier, and used a virtual drag and lift formulation to capture the impact of fluid inflow on the actuator loads.

In Section IV the combined ship motion model was calibrated and validated towards sea trials, showing good agreement with numerical simulations and experimental data.

The model calibration focused on a time period when RVG was operated at cruising speed with moderate actuator commands. Yet, the model was able to replicate the recorded ship motions with reasonably accuracy for the full set of operating conditions considered during sea trials. Justified by its basis in physical principles, the 4DOF maneuvering model is expected to have a large validity range, perhaps even extending beyond the sea trials data set. However, the actuator model cannot be expected valid beyond the calibration data, limiting the overall validity range of the ship motion model.

B. ONLINE DSS SOLUTIONS

As an illustration of possible applications of the ship motion model, two conceptual DSS solutions were investigated. The CADCA DSS solution of Section V used the predicted ship trajectories under pre-defined actuator commands to determine the critical navigation area for selected encounter scenarios.

In Section VI, a novel guidance control design was developed, using CBFs for collision avoidance capabilites. It was then proposed to use the guidance controller as a virtual autopilot for the ship motion model, in order to predict the future ship trajectory during operation. The CBF-based DSS solution is currently at a conceptual level, and maturing of the virtual autopilot is required. In particular, further development is needed to ensure satisfactory COLREG-compliance.

Despite the good agreement between model and sea trials trajectories, there is inherent uncertainty in the ship motions predicted by the numerical model. Moreover, the ship motion model does not include wind and wave disturbances, whereas estimates of current conditions may not be available during operation. For the aforementioned reasons, a suitable safety margin towards model uncertainty should be included in both DSS solutions before deployment.

VIII. CONCLUDING REMARKS

The aim of this study was to contribute towards the development of MASS solutions. To this end, a pragmatic numerical ship motion model of RVG was presented, consisting of two submodels; a 4DOF manuevering model, and an actuator model. Validation towards a sea trials dataset revealed that the model predicts the ship motions with reasonably accuracy over a large range of forward speeds and turning maneuvers. A major significance of the research lies in the combination of a maneuvering model and an actuator model, where both models are of high fidelity. Future work may include an improvement of the actuator model, which may also trigger a refinement of the maneuvering model parameters. Augmenting the model with wind and wave loads will further enhance the value of the model as a tool for DSS development and testing. The obtained agreement between the simulated and sea trials trajectories justifies the use of the model in onboard DSS. For the CBF-based DSS concept of Section VI, a systematic procedure for selecting the target ship critical area for different encounter situations is required before deployment. A promising solution, currently under investigation, is using the CADCA database to determine suitable target ship critical area.

REFERENCES

[1] Z. H. Munim, "Autonomous ships: A review, innovative applications and future maritime business models," *Supply Chain Forum, Int. J.*, vol. 20, no. 4, pp. 266–279, Oct. 2019.
[2] O. Smogeli, "Digital twins at work in maritime and energy," DNV, Høvik, Norway, Tech. Rep., 2017.
[3] W. Gierusz, "Simulation model of the LNG carrier with podded propulsion Part 1: Forces generated by pods," *Ocean Eng.*, vol. 108, pp. 105–114, Nov. 2015.
[4] W. Gierusz, "Simulation model of the LNG carrier with podded propulsion, Part II: Full model and experimental results," *Ocean Eng.*, vol. 123, pp. 28–44, Sep. 2016.
[5] D. Mu, G. Wang, Y. Fan, and Y. Zhao, "Modeling and identification of podded propulsion unmanned surface vehicle and its course control research," *Math. Problems Eng.*, vol. 2017, pp. 1–13, Jan. 2017.
[6] X. Sun, G. Wang, Y. Fan, D. Mu, and B. Qiu, "Collision avoidance of podded propulsion unmanned surface vehicle with COLREGs compliance and its modeling and identification," *IEEE Access*, vol. 6, pp. 55473–55491, 2018.
[7] P. S. Kleppe and H. V. Lien. *Intelligent Systems Lab, NTNU Ålesund*. Accessed: Feb. 24, 2023. [Online]. Available: https://org.ntnu.no/intelligentsystemslab/gunnerus.html
[8] R. Skjetne, M. E. N. Sørensen, M. Breivik, S. A. T. Værnø, A. H. Brodtkorb, A. J. Sørensen, Ø. K. Kjerstad, V. Calabro, and B. O. Vinje, "AMOS DP research cruise 2016: Academic full-scale testing of experimental dynamic positioning control algorithms onboard R/V Gunnerus," in *Proc. ASME Int. Conf. Ocean, Offshore Arctic Eng.*, Jun. 2017, pp. 1–10.
[9] *RV Gunnerus Home Page*. Accessed: Feb. 24, 2023. [Online]. Available: https://www.ntnu.edu/oceans/gunnerus
[10] *RV Horyzont II Home Page*. Accessed: Feb. 24, 2023. [Online]. Available: https://umg.edu.pl/en/horyzont-II
[11] H. Zhang, G. Li, L. I. Hatledal, Y. Chu, A. L. Ellefsen, P. Han, P. Major, R. Skulstad, T. Wang, and H. P. Hildre, "A digital twin of the research vessel *Gunnerus* for lifecycle services: Outlining key technologies," *IEEE Robot. Autom. Mag.*, early access, Nov. 14, 2022, doi: 10.1109/MRA.2022.3217745.
[12] V. Hassani, A. Ross, O. Selvik, D. Fathi, F. Sprenger, and T. E. Berg, "Time domain simulation model for research vessel Gunnerus," in *Proc. OMAE*, 2015, pp. 1–6.
[13] A. Ross, V. Hassani, O. Selvik, E. Ringen, and D. Fathi, "Identification of nonlinear manoeuvring models for marine vessels using planar motion mechanism tests," in *Proc. Int. Conf. Offshore Mech. Arctic Eng.*, 2015, pp. 1–7.
[14] O. M. Faltinsen, *Sea Loads on Ships and Offshore Structures*. Cambridge, U.K.: Cambridge Univ. Press, 1993.
[15] O. M. Faltinsen, *Hydrodynamics of High-Speed Marine Vehicles*. Cambridge, U.K.: Cambridge Univ. Press, 2005.
[16] T. I. Fossen, *Handbook of Marine Craft Hydrodynamics and Motion Control*. Hoboken, NJ, USA: Wiley, 2011.
[17] Ø. Rabliås and T. Kristiansen, "A 2D+t approach for the transverse viscous loads in a modular maneuvering model," *Ocean Eng.*, vol. 228, May 2021, Art. no. 108853.
[18] H. Yasukawa, R. Sakuno, and Y. Yoshimura, "Practical maneuvering simulation method of ships considering the roll-coupling effect," *J. Mar. Sci. Technol.*, vol. 24, no. 4, pp. 1280–1296, Dec. 2019.
[19] M. Gil, "A concept of critical safety area applicable for an obstacle-avoidance process for manned and autonomous ships," *Rel. Eng. Syst. Saf.*, vol. 214, Oct. 2021, Art. no. 107806.
[20] M. Gil, J. Montewka, P. Krata, T. Hinz, and S. Hirdaris, "Determination of the dynamic critical maneuvering area in an encounter between two vessels: Operation with negligible environmental disruption," *Ocean Eng.*, vol. 213, Oct. 2020, Art. no. 107709.
[21] M. Marley, R. Skjetne, M. Breivik, and C. Fleischer, "A hybrid kinematic controller for resilient obstacle avoidance of autonomous ships," *IOP Conf. Ser., Mater. Sci. Eng.*, vol. 929, no. 1, Nov. 2020, Art. no. 012022.

[22] M. Marley, R. Skjetne, and A. R. Teel, "Synergistic control barrier functions with application to obstacle avoidance for nonholonomic vehicles," in *Proc. Amer. Control Conf. (ACC)*, New Orleans, LA, USA, May 2021, pp. 243–249.

[23] M. Marley, R. Skjetne, E. Basso, and A. R. Teel, "Maneuvering with safety guarantees using control barrier functions," *IFAC-PapersOnLine*, vol. 54, no. 16, pp. 370–377, 2021.

[24] *Stack Exchange: Drawing Figure of a Boat With the Tikz-Package*. Accessed: Jun. 7, 2023. [Online]. Available: https://tex.stackexchange.com/a/226690

[25] *Open Simulation Platform*. Accessed: Feb. 24, 2023. [Online]. Available: https://opensimulationplatform.com

[26] M. Gil, J. Montewka, P. Krata, and T. Hinz, "Ship stability-related effects on a critical distance of collision evasive action," in *Proc. 17th Int. Ship Stability Workshop*, Helsinki, Finland, 2019, pp. 231–238.

[27] C. Guo and I. B. Utne, "Development of risk indicators for losing navigational control of autonomous ships," *Ocean Eng.*, vol. 266, Dec. 2022, Art. no. 113204.

[28] K. Wróbel, M. Gil, P. Krata, K. Olszewski, and J. Montewka, "On the use of leading safety indicators in maritime and their feasibility for maritime autonomous surface ships," *Proc. Inst. Mech. Eng., O, J. Risk Rel.*, vol. 237, no. 2, pp. 314–331, Apr. 2023.

[29] M. Abilio Ramos, I. B. Utne, and A. Mosleh, "Collision avoidance on maritime autonomous surface ships: Operators' tasks and human failure events," *Saf. Sci.*, vol. 116, pp. 33–44, Jul. 2019.

[30] R. Szlapczynski and J. Szlapczynska, "A ship domain-based model of collision risk for near-miss detection and collision alert systems," *Rel. Eng. Syst. Saf.*, vol. 214, Oct. 2021, Art. no. 107766.

[31] T. G. Coldwell, "Marine traffic behaviour in restricted waters," *J. Navigat.*, vol. 36, no. 3, pp. 430–444, Sep. 1983.

[32] A. D. Ames, S. Coogan, M. Egerstedt, G. Notomista, K. Sreenath, and P. Tabuada, "Control barrier functions: Theory and applications," in *Proc. 18th Eur. Control Conf. (ECC)*, Napoli, Italy, Jun. 2019, pp. 3420–3431.

[33] E. H. Thyri, E. A. Basso, M. Breivik, K. Y. Pettersen, R. Skjetne, and A. M. Lekkas, "Reactive collision avoidance for ASVs based on control barrier functions," in *Proc. IEEE Conf. Control Technol. Appl. (CCTA)*, Aug. 2020, pp. 380–387.

[34] M. Marley, R. Skjetne, and A. R. Teel, "A kinematic hybrid feedback controller on the unit circle suitable for orientation control of ships," in *Proc. 59th IEEE Conf. Decis. Control (CDC)*, Dec. 2020, pp. 1523–1529.

[35] W. Xiao and C. Belta, "Control barrier functions for systems with high relative degree," in *Proc. IEEE 58th Conf. Decis. Control (CDC)*, Nice, France, Dec. 2019, pp. 474–479.

[36] W. Xiao and C. Belta, "High-order control barrier functions," *IEEE Trans. Autom. Control*, vol. 67, no. 7, pp. 3655–3662, Jul. 2022.

MATHIAS MARLEY (Member, IEEE) received the M.Sc. degree in marine control engineering from the Department of Marine Technology, Norwegian University of Science and Technology (NTNU), in 2014, specializing in marine cybernetics. He is currently pursuing the Ph.D. degree with the Centre for Autonomous Marine Operations and Systems (SFF AMOS), NTNU.

Before his Ph.D. studies, he was employed by engineering consultancy firms COWI and Dr.Techn.Olav Olsen, where he worked on various offshore renewable energy and infrastructure projects, mainly within the fields of hydrodynamics, aerodynamics, and structural dynamics. He is currently a Researcher with the Offshore Wind Division, Norwegian state-owned energy company Equinor. His research interest includes nonlinear and hybrid motion control of autonomous marine vessels.

ROGER SKJETNE (Senior Member, IEEE) received the M.Sc. degree in control engineering from the University of California at Santa Barbara (UCSB), in 2000, and the Ph.D. degree from the Norwegian University of Science and Technology (NTNU), in 2005.

Before his studies, he was a Certified Electrician with Aker Elektro AS on numerous oil installations for the North Sea. From 2004 to 2009, he was employed with Marine Cybernetics AS, working on a hardware-in-the-loop simulation for testing marine control systems. Since August 2009, he has been the Kongsberg Maritime Chair Professor of marine control engineering with the Department of Marine Technology, NTNU. From 2017 to 2018, he was a Visiting Research Scholar with the Center for Control, Dynamical-Systems and Computation, UCSB. His research interests include autonomous ship guidance and control, dynamic positioning of marine vessels, control of shipboard hybrid-electric power systems, Arctic station keeping and ice management systems, and nonlinear and adaptive motion control of marine vessels in general. He holds an Exxon Mobil Prize for his Ph.D. thesis with NTNU.

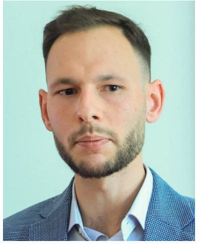

MATEUSZ GIL received the B.Sc. and M.Sc. degrees in navigation from Gdynia Maritime University (GMU), with a particular focus on maritime transportation and offshore technologies. He is currently pursuing the Ph.D. degree with the Department of Navigation, GMU, with a focus on ship collision avoidance. During his studies with GMU, he obtained the Officer of the Watch (OOW) license, which allowed him to work at sea on board merchant ships after graduation. He is employed as a Research Assistant with the Department of Navigation, GMU. His main research interests include issues related to maritime transportation risk and safety, autonomous shipping, as well as maritime education and training.

PRZEMYSLAW KRATA received the Ph.D. degree from the Szczecin University of Technology, in 2008, and the D.Sc. degree from Gdynia Maritime University, in 2018. His scientific interests relate to ship operations comprising mainly stability issues and collision avoidance, thus contributing to the safety of navigation. Holding the watchkeeping officer license, he combined academic duties with seafaring in the first years of his professional career, thus gaining some sea experience and allowing for his awareness of the practical problems related to the ship's operation. Time spent on board still benefits his research and teaching expertise since it often brings him to realistic and applicable solutions to the problems emerging in the field of marine navigation.

• • •